ACS APPLIED MATERIALS & INTERFACES

www.acsami.org

Research Article

In_2O_3:H-Based Hole-Transport-Layer-Free Tin/Lead Perovskite Solar Cells for Efficient Four-Terminal All-Perovskite Tandem Solar Cells

Somayeh Moghadamzadeh, Ihteaz M. Hossain, Moritz Loy, David Benedikt Ritzer, Hang Hu, Dirk Hauschild, Adrian Mertens, Jan-Philipp Becker, Amir A. Haghighirad, Erik Ahlswede, Lothar Weinhardt, Uli Lemmer, Bahram Abdollahi Nejand,* and Ulrich W. Paetzold*

Cite This: https://doi.org/10.1021/acsami.1c06457

Read Online

ACCESS | Metrics & More | Article Recommendations | Supporting Information

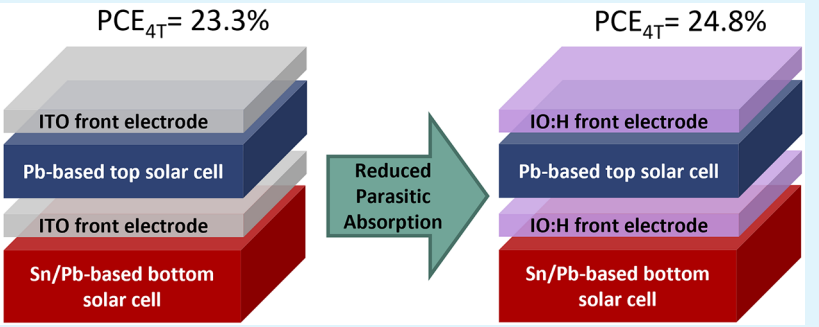

ABSTRACT: Narrow-band gap (NBG) Sn−Pb perovskites with band gaps of ∼1.2 eV, which correspond to a broad photon absorption range up to ∼1033 nm, are highly promising candidates for bottom solar cells in all-perovskite tandem photovoltaics. To exploit their potential, avoiding optical losses in the top layer stacks of the tandem configuration is essential. This study addresses this challenge in two ways (1) removing the hole-transport layer (HTL) and (2) implementing highly transparent hydrogen-doped indium oxide In_2O_3:H (IO:H) electrodes instead of the commonly used indium tin oxide (ITO). Removing HTL reduces parasitic absorption loss in shorter wavelengths without compromising the photovoltaic performance. IO:H, with an ultra-low near-infrared optical loss and a high charge carrier mobility, results in a remarkable increase in the photocurrent of the semitransparent top and (HTL-free) NBG bottom perovskite solar cells when substituted for ITO. As a result, an IO:H-based four-terminal all-perovskite tandem solar cell (4T all-PTSCs) with a power conversion efficiency (PCE) as high as 24.8% is demonstrated, outperforming ITO-based 4T all-PTSCs with PCE up to 23.3%.

KEYWORDS: *perovskite solar cells, narrow-band gap, parasitic absorption, IO:H transparent electrodes, all-perovskite tandem, perovskite−perovskite tandem, low-band gap*

Downloaded via KIT BIBLIOTHEK on September 27, 2021 at 08:58:36 (UTC).
See https://pubs.acs.org/sharingguidelines for options on how to legitimately share published articles.

INTRODUCTION

The state-of-the-art single-junction organic−inorganic Pb-based perovskite solar cells (PSCs) with a certified power conversion efficiency (PCE) of 25.5%[1] are restricted to the theoretical detailed balance efficiency limits (31−33%).[2] However, tandem architectures composed of a wide-band gap (WBG) top solar cell and a narrow-band gap (NBG) bottom solar cell can overcome the detailed balance limits of the single-junction PSCs. So far, most studies have focused on pure Pb-based PSCs with wide-band gaps (∼1.6 eV) and their application as the top subcell in perovskite/Si tandem solar cells.[3−7] However, by partially replacing Pb with Sn in metal-halide perovskite absorbers, it is possible to tune their band gap to lower values (∼1.2 eV) and design NBG PSCs to be used as new candidates for the bottom subcell in tandem solar cell configurations.[8−15]

Despite the shortage of studies, with recent advances, NBG mixed Sn−Pb PSCs possess reasonable efficiencies (∼20%).[8−10,12,16,17] To date, all-perovskite tandem solar cells (all-PTSCs) with certified PCEs of 25.4% (for four-terminal)[9] and 24.8% (for two-terminal)[10] have been promoted as a possible solution to surpass the detailed balance limits of the single-junction PSCs while benefiting from low-temperature and low-cost fabrication methods. However, for attaining all-PTSCs with efficiencies >30%, the NBG mixed Sn−Pb PSCs are still required to provide efficiencies of at least 21−22%.

Received: April 8, 2021
Accepted: August 9, 2021

© XXXX The Authors. Published by American Chemical Society

Therefore, further intensive research efforts and new strategies are desirable for improving the single-junction NBG PSCs.

To date, the ideal choice for the hole-transport layer (HTL) of NBG mixed Sn−Pb PSCs are still under debate. Although PSCs with inorganic NiO_x HTL are very promising, they lack reproducibility, given that the exact conditions of processing are important for determining the oxidation state of NiO_x.[18] Polyethylenedioxythiophene:polystyrenesulfonate (PEDOT:PSS) and poly[bis(4-phenyl)(2,4,6-trimethylphenyl)amine] (PTAA), which are common organic HTLs used in the p−i−n mixed Sn−Pb PSCs, have other shortcomings.[12,16,17,19,20] The interface between the PEDOT:PSS and mixed Sn−Pb perovskite absorber was evidenced to cause device instabilities and charge extraction deterioration after thermal aging at 85 °C.[21] Replacing PEDOT:PSS with PTAA boosts the open-circuit voltage (V_{OC}) with improved thermal stability such that the PSCs maintain 80% of their initial power efficiency after 4000 h at 85 °C.[22] Despite the advances of PTAA-based devices, the strong hydrophobicity of PTAA is a big challenge that causes unwanted perovskite morphologies and issues with device reproducibility.[23,24] Furthermore, PTAA degrades under prolonged ultraviolet (UV) light exposure leading to an increase in defect density, and therefore, an overall reduction in the charge carrier extraction.[25] Moreover, PTAA and PEDOT:PSS introduce unwanted parasitic absorption loss in shorter and longer wavelengths, respectively, which limits external quantum efficiency (EQE) of the respective PSCs.[26]

Recently, PSCs without charge transport layers are proved to demonstrate high performance.[27] In particular, hole-transport-layer-free (HTL-free) PSCs, with NBG mixed Sn−Pb perovskite absorbers deposited directly onto indium tin oxide (ITO), are realized to attain high PCEs.[21,22,27,28] Prasanna et al. reported on HTL-free PSCs with PCEs up to 16.4% (with only ≈0.2% absolute drop in efficiency compared to less-stable PEDOT:PSS PSCs) and 95% of their initial efficiency under damp heat aging for 1000 h at 85 °C in air.[21] Despite the lack of selective contact, a V_{OC} of 0.7 V and a high short-circuit current (J_{SC}) of 30.2 mA/cm^2 were observed.

Band bending at the ITO/perovskite interface has been reported to efficiently facilitate charge extraction at this interface even in the absence of a charge transport layer.[27] The Fermi level of a mixed Sn−Pb perovskite material is above that of ITO.[21,27] One hypothesis is that the charge carriers redistribute in the perovskite near the ITO/perovskite interface to line up the Fermi levels across the ITO/perovskite heterojunction at equilibrium. This results in an upward band bending of the energy levels of the mixed Sn−Pb perovskite.[21,27] As a result, a spatially electrostatic potential builds up across this interface that extracts holes from the perovskite to ITO, while blocking the electrons and therefore preventing their recombination with holes in the ITO.[27] The resulting upward band bending rationalizes how HTL-free PSCs attain high PCEs. Notably, simplifying the structure by removing the HTL does not impede the stability of the PSCs, regardless of the perovskite composition.[21,29−31] Moreover, simplifying device fabrication reduces the number of processing steps and accordingly the fabrication cost, which is one of the hurdles toward commercialization of this technology.[32]

Parasitic absorption loss in the near-infrared (NIR) region, introduced by transparent conductive oxide (TCO) front electrodes, is particularly disadvantageous for NBG mixed Sn−Pb PSCs with NIR band gaps of ∼1.2 eV and a favorable photon absorption up to 1033 nm. Thereby, it is essential to exploit this benefit of NBG PSCs to potentially serve the need for higher performance as a bottom subcell in all-PTSCs. Hydrogen-doped indium oxide In_2O_3:H (IO:H) thin films with high carrier mobility and NIR absorptance of only 2% are ideal candidates for NBG PSCs and tandem configurations.[33,34] It has been successfully used in Si heterojunction solar cells,[35,36] CIGS solar cells,[37,38] and in the top subcell in perovskite/Si and perovskite/CIGS tandem configurations.[39−41] Moreover, IO:H is reported to have excellent thermal and chemical stability for solar cell applications.[38]

In this work, we explore the potential of IO:H as a front electrode for HTL-free NBG PSCs for the first time. We also demonstrate that IO:H is not only as compatible as ITO for HTL-free NBG PSCs but also a better choice since there are fewer Sn^{4+} at the IO:H/perovskite interface. Furthermore, for the first time, we report on the performance of four-terminal (4T) all-PTSCs, for which both subcells (semitransparent top and HTL-free bottom) have IO:H front electrodes. Comparing ITO-based 4T all-PTSCs as a reference with IO:H-based 4T all-PTCSs, we realize a significant improvement in PCEs from 23.3 to 24.8%. Optical characterization reveals that this enhancement stems from a remarkably enhanced transmittance of the semitransparent top and HTL-free NBG bottom perovskite subcells.

RESULTS AND DISCUSSION

In line with the literature,[26] we show that PTAA, which is a widely used HTL in NBG PSCs with p−i−n structures, introduces unwanted parasitic absorption in the shorter wavelength region and therefore leads to a reduced EQE. Figure 1 exhibits spectrophotometric measurements for glass/ITO/PTAA/air (red) and glass/ITO/air (dark gray). It is apparent that coating ITO with PTAA (here 6 nm) results in

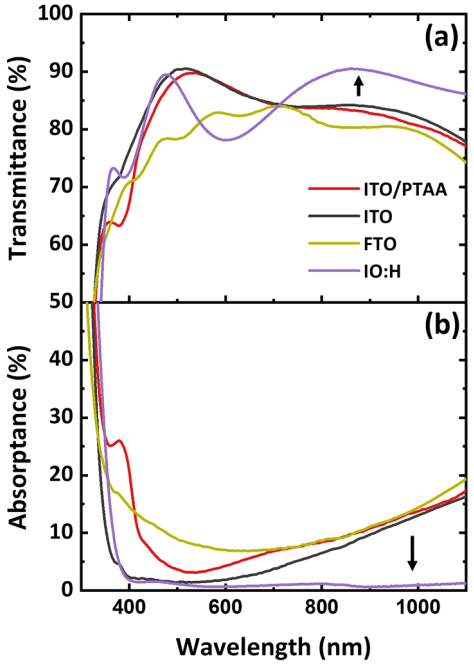

Figure 1. (a) Transmittance and (b) absorptance spectra of glass substrates coated with ITO/PTAA, ITO (140 nm), fluorine-doped tin oxide (FTO) (550 nm), and IO:H (230 nm).

https://doi.org/10.1021/acsami.1c06457
ACS Appl. Mater. Interfaces XXXX, XXX, XXX−XXX

increased absorption loss and reduced transmittance mainly in the wavelength range of 350−500 nm. Figure S1a illustrates the layer stack of a PSC with an NBG perovskite absorber layer of composition $Cs_{0.025}(FA_{0.8}MA_{0.2})_{0.975}Sn_{0.5}Pb_{0.5}I_3$, with a band gap of 1.26 eV.[20] We realize that the photovoltaic (PV) performance of this stack with and without PTAA HTL is comparable. A remarkable enhancement in the EQE responses for shorter wavelength (≈350−500 nm) for the HTL-free architecture results in an increase in the integrated J_{SC} (by ≈0.5 mA/cm^2) calculated from the EQE spectra (Figure S1b). Above 500 nm, both devices show similar EQE responses indicating that the quality of the perovskite thin film and the interface is not significantly altered when deposited directly on bare ITO. The current enhancement, which is attributed to lower absorption in the absence of PTAA, is also observed in the current density vs voltage (J−V) scans (Figure S1c), where the J_{SC} improves from 27.9 mA/cm^2 for the PSC with PTAA to 28.3 mA/cm^2 for the HTL-free PSC. An improvement in the fill factor (FF) is evidenced as well, which, as discussed earlier, could be associated with favorable band bending at the ITO/perovskite interface.[21,27] We notice that the V_{OC} of the HTL-free PSC (0.798 mV) is comparable to that of a PTAA-based device (0.811 mV). It is known that V_{OC} and FF of PSCs are closely related to the ratio of nonradiative and interface recombination.[42] Therefore, in agreement with the literature,[21] we hypothesize that the band bending at the ITO/perovskite interface helps in reducing nonradiative recombination at this interface. Interestingly, removing PTAA is not detrimental to the stabilized PCE (SPCE) as measured under maximum power point (MPP) tracking conditions (Figure S1d).

Apart from the HTL, parasitic absorption in the NIR region introduced by common TCOs such as ITO and fluorine-doped tin oxide (FTO) is also disadvantageous, specifically for NBG PSCs with a NIR band gap of ∼1.2 eV. Figure 1, presents the spectral transmittance and absorptance of a glass/TCO/air structure, for ITO (Luminescence Technology), FTO (Sigma Aldrich), and IO:H (in-house sputtered, see Table S1 for details)[40] TCOs. IO:H with an improved transmittance in the NIR region (700−1100 nm) demonstrates the lowest (<2%) absorptance compared to that of commercial ITO and FTO. However, optical analysis reveals an approximately overall higher reflection loss for IO:H due to its higher refractive index (n) compared to ITO and FTO; see Figures S2a and S2b. A higher refractive index (n) of IO:H corresponds to a smaller refractive index contrast between IO:H and the NBG mixed Sn−Pb perovskite absorber layer, particularly at the band gap (see Figure S2b; the refractive index demonstrated for the mixed Sn/Pb perovskite agrees with the literature[43]). The smaller refractive index contrast between the IO:H front electrode and NBG mixed Sn/Pb perovskite is expected to favorably reduce the Fresnel reflection loss at the IO:H/perovskite interface. In agreement with the absorptance, the extinction coefficient (k) is quite low in the NIR wavelengths for IO:H, compared to ITO and FTO (Figure S2c). Furthermore, the optical band gap (E_g) of IO:H is slightly lower (∼0.1 eV) than that of ITO and FTO, as derived from the Tauc plots (Figure S2d). This reduction in the band gap should lead to only 0.1 mA/cm^2 reduction in the J_{SC} (absorptance weighted with AM 1.5G spectra between 300 and 400 nm), which does not affect the performance of the respective PSCs significantly.

The electrical properties of the TCOs are fundamentally interlinked with their optical performances (see Table 1). The reduced extinction coefficient (k) or, in other words, the low NIR absorptance of IO:H is related to its significantly lower charge carrier concentration (n_c) because the free carriers absorb photons mostly in the NIR wavelengths (lower energies).[40] The low charge carrier concentration (n_c), however, comes at a cost of low conductivity, accompanied by a higher sheet resistance (R_{sq}) compared to the commercial ITO and FTO (Table 1). However, remarkably high mobility (μ) of IO:H maintains sufficient conductivity, compensating for the low charge carrier concentration (n_c).

Table 1. Layer Thickness (d), Optical Band gap (E_g), Charge Carrier Concentration (n_c), Sheet Resistance (R_{sq}), Charge Carrier Mobility (μ), and Surface Roughness (S_{rms}) of the Front Transparent Conductive Oxide (TCO) Electrodes: Indium Tin Oxide (ITO), Fluorine-Doped Tin Oxide (FT), and Hydrogen-Doped Tin Oxide (IO:H)

TCO	ITO	FTO	IO:H
d (nm)	140	550	230
E_g (eV)	3.95	3.99	3.87
n_c (1/cm^3)	10.5 × 10^{20}	10.5 × 10^{20}	1.7 × 10^{20}
R_{sq} (Ω/sq)	15	7	23
μ (cm^2/Vs)	35.1 ± 3.9	36.3 ± 3.8	85.8 ± 1.2
S_{rms} (nm)	3 ± 1	15 ± 5	<1

The thickness (d) of a TCO electrode affects the optical and electrical properties of the solar cell. Apart from higher mobility (μ), a thicker layer can compensate for the low charge carrier concentration (n_c) and induce a desirable decrease in the sheet resistance ($R_{sq} \approx 1/e\, n_c\, \mu\, d$). A thinner layer, on the other hand, might be beneficial for lower absorption, although it leads to a strong increase in the sheet resistance (R_{sq}). We previously performed semiempirical studies to determine the thickness of IO:H that allows for an optimal balance between optical and electrical losses.[44] Based on our findings, the optimum thickness of sputtered IO:H is more dominated by its electrical rather than optical properties. Overall, an IO:H layer with an optimum thickness of 230 nm simultaneously lowers the sheet resistance and does not exhibit high parasitic absorption in the NIR region. A shift in the maximum of the interference in the transmittance and reflectance spectra of the TCO layers is due to the inevitable different thicknesses of the TCO layers.

On performing atomic force microscopy (AFM) in tapping mode on the three different TCOs (Figure S3), we recapitulate that IO:H has a surface roughness of only 1 nm, which could enhance nucleation of the perovskite thin film. FTO, on the other hand, has the highest surface roughness among the three TCOs (15 ± 5 nm), which may be beneficial for better light scattering at the TCO/perovskite interface. Moreover, we characterize the crystallinity of the three TCOs using X-ray diffraction (XRD) characterization (Figure S4a). In line with the literature, ITO and IO:H TCOs are crystalline with preferential orientation along their (222) planes,[40] whereas FTO is crystalline with a dominant orientation along its (110) plane.[45] The high crystallinity of IO:H observed from the XRD measurements is indicative of larger crystallites compared to the commercial ITO. An analysis on the XRD reflection peaks of the TCOs (see the Supporting Information for details) confirms that, compared to the commercial ITO, the in-house sputtered IO:H layer possesses considerably sharper reflection peaks with reduced full width at half-maximum (FWHM) and larger crystallites (Table S2). This high crystallinity could be

https://doi.org/10.1021/acsami.1c06457
ACS Appl. Mater. Interfaces XXXX, XXX, XXX−XXX

associated with the post-thermal treatment, which crystallizes the amorphous IO:H deposited at the time of sputtering.[40] The high crystallinity of IO:H improves the IO:H/perovskite interface and accordingly the charge transport at this interface. We used the Scherrer equation for our analysis (see the Supporting Information for details), which applies when broadening in the FWHM due to microstrain can be neglected.

In general, substrates have an impact on the morphology and the quality of the perovskite thin films, both of which influence the performance of the respective PSCs.[46] XRD measurements (Figure S4b) detect two dominant peaks for the NBG perovskite thin films deposited on ITO, FTO, and IO:H. These peaks at 14.1 and 28.3° are, respectively, assigned to the (002)/(110) and (004)/(220) planes of the tetragonal perovskite crystal structure, independent of the three investigated TCOs.[47] The intensities of these two peaks differ for different TCOs, denoting that the crystallinity of the perovskite thin films is different. Sharper peaks in the perovskite XRD patterns, which correlate with larger grains as evidenced by scanning electron microscopy (SEM) images (Figure S5), indicate that ITO and IO:H are potentially more suitable substrates for perovskite thin films with advanced crystallinity, compared to FTO. The perovskite films deposited on ITO and IO:H have slightly larger grains, and therefore, fewer grain boundaries leading to reduced nonradiative recombination, according to some studies.[48−51]

Apart from the quality of a perovskite thin film, which is directly fabricated onto the TCOs in the HTL-free devices, the impact of the TCO substrate on the interface of the TCO/perovskite is also critical for high-performance PSCs.[52−57] Here, we investigate three different sets of samples using X-ray photoelectron spectroscopy (XPS) to analyze the chemical and electronic structures of the TCO/perovskite interface: (1) TCO, (2) TCO coated with a thin NBG perovskite (≈3 nm), and (3) TCO coated with a thick NBG perovskite (600 nm, i.e., the nominal thickness) films, with ITO, FTO, or IO:H TCOs. In the XPS survey spectra of these samples (Figure S6), all expected TCO signals are detected and attenuated with increasing perovskite thickness. The spectra of the thick perovskite films on different TCOs exhibit all-perovskite-related peaks, which are very similar indicating that the influence of the TCO on the chemical structure of the perovskite films is small.

The beginning of the growth of the perovskite on the TCOs is analyzed using thin NBG perovskite films. For this, we derive the thickness of the perovskite film from the attenuation of XPS line of the TCO substrate assuming a perovskite film with homogeneous thickness. As summarized in Figure S7, we find a thickness of (2 ± 1) nm for the "thin" perovskite on ITO and FTO. In contrast, the derived thickness for the IO:H substrates is approx. twice as large [(5 ± 2) nm], which indicates a faster or more homogeneous growth of the perovskite film on IO:H and is consistent with the AFM results in Figure S3.

The spectral shapes of the XPS lines give us further information on the chemical species present at the interface. For the Sn $3d_{5/2}$ of all three thick perovskite samples (green lines in Figure 2), we find a slight asymmetry, which can be related to a small contribution from Sn^{4+}.[19] For ITO and FTO (blue lines in Figure 2), the Sn $3d_{5/2}$ peak is found at binding energies of 486.7 and 487.0 eV, respectively, while no Sn-related intensity is detected for the IO:H sample. To analyze the thin perovskite, we have tried to reproduce their Sn $3d_{5/2}$ signals (open circles in Figure 2) by a weighted sum of the spectra of the respective TCO substrate and the corresponding thick perovskite. We find that the spectra of the ITO/thin perovskite and FTO/thin perovskite can be well reproduced using this approach as shown in Figure 2. In contrast, the Sn $3d_{5/2}$ signal of the IO:H/thin perovskite sample cannot be reproduced, as the Sn $3d_{5/2}$ signal of the thin perovskite consists of only one spectral component indicative of an Sn^{2+} environment (while the substrate exhibits no Sn signal, the thick perovskite exhibits Sn^{2+} and some Sn^{4+} signals). This result suggests that the NBG perovskite on Sn(−O) free substrate benefits from less oxidation at the beginning of the growth, which could be beneficial for the stability of the solar cells and possibly for the charge carrier transport.

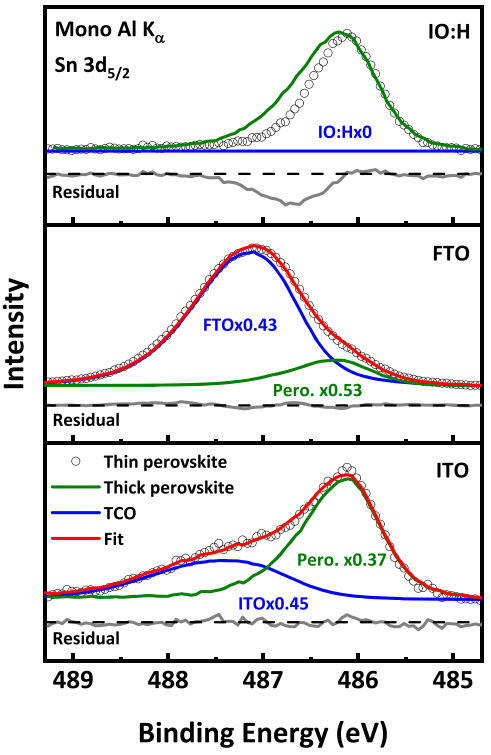

Figure 2. Monochromatized Al K_α spectra (open circles) of the Sn $3d_{5/2}$ region of the thin narrow-band gap perovskite for IO:H, FTO, and ITO substrate (from top to bottom, respectively). Fits (red) are shown describing the spectra as a weighted sum of the substrate (blue) and thick perovskite (green) spectra. Underneath each spectrum, the residuum is shown in gray.

To analyze the impact of the type of TCO on the band bending changes induced by the TCO/NBG perovskite interface, we determine the energy shifts of the most prominent XPS core levels, which are exclusively present in the NBG perovskite films (i.e., Cs 3d, I 3d, N 1s, C 1s, and Pb 4f). As seen in Figure S8, peak shifts between the thin and thick perovskite layers are generally small. An exception is the lower binding energy region in the C 1s spectra, where strong spectral changes are observed that can be attributed to different C species. Excluding this region, the average shifts of all XPS levels are +0.06 ± 0.04 eV for ITO, 0.01 ± 0.03 eV for IO:H, and −0.04 ± 0.04 eV for FTO, when going from the thin to the thick perovskite film. This suggests that changing the type of TCO has little impact on band bending in the perovskite film. Overall, the XPS results suggest a faster start of the growth of the NBG perovskite and reduced Sn^{4+} formation at the IO:H/perovskite interface than with ITO and FTO.

https://doi.org/10.1021/acsami.1c06457
ACS Appl. Mater. Interfaces XXXX, XXX, XXX−XXX

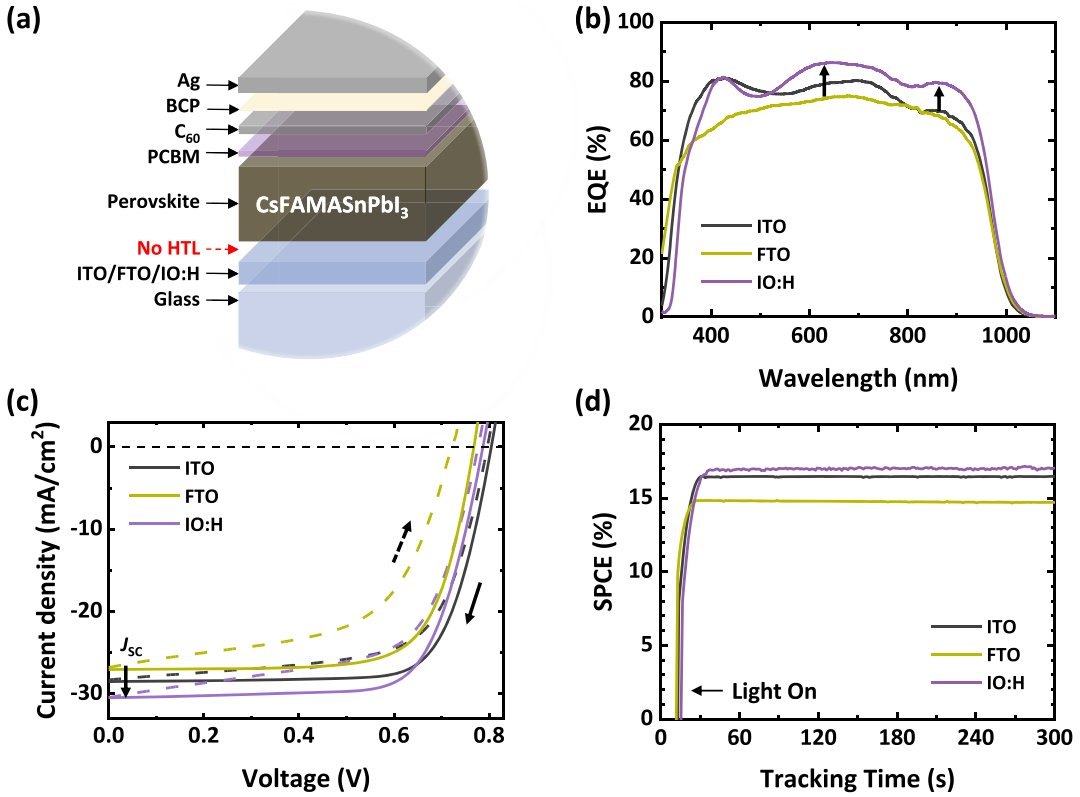

Figure 3. (a) Schematic of the layer stack, (b) external quantum efficiency (EQE) spectra, (c) current density vs voltage (J–V) scans (the rate of voltage sweep was fixed at 0.6 V/s in both backward ($V_{OC} \rightarrow J_{SC}$; solid lines) and forward ($J_{SC} \rightarrow V_{OC}$; dashed lines) scans), and (d) stabilized power conversion efficiency (SPCE) from the maximum power point tracking measurements of the HTL-free narrow-band gap PCSs with $Cs_{0.025}(FA_{0.8}MA_{0.2})_{0.975}Sn_{0.5}Pb_{0.5}I_3$ perovskite absorber layers deposited directly on commercial ITO, commercial FTO, and in-house sputtered IO:H front electrodes. The measurement was performed under standard test conditions (100 mW/cm^2, 25 °C).

Having demonstrated that the optical properties of IO:H are significantly improved compared to the commonly used ITO and FTO, we determine how they correlate to the PV performance of the respective PSCs. As illustrated in Figure 3a, we fabricate three sets of HTL-free NBG PSCs with a layer sequence of glass/TCO/$Cs_{0.025}(FA_{0.8}MA_{0.2})_{0.975}Sn_{0.5}Pb_{0.5}I_3$/phenyl-$C_{61}$-butyric acid methyl ester (PCBM)/buckminsterfullerene (C_{60})/bathocuproine (BCP)/silver (Ag), for which the TCO differs from ITO to FTO and IO:H. Figure 3b–d depicts the PV performance of the champion PSCs with different TCOs. There is a clear improvement in the EQE spectrum (Figure 3b) of the IO:H-based PSC over a broad wavelength region ranging from 520 to 950 nm (band gap of the mixed Sn–Pb perovskite thin film) compared to the ITO- and FTO-based PSCs. This increase stems from the lower parasitic absorption loss (higher transmittance) as well as the reduced reflection losses originating from the increased refractive index of the IO:H, as discussed earlier. The EQE response of the FTO-based PSC shows an overall reduction between 350 and 800 nm due to the high absorptance of the FTO substrate in this region (Figure 1b). Overall, the integrated J_{SC} derived from the EQE responses (Figure 3b) confirms an improvement from 27.5 mA/cm^2 (for the ITO-based PSC) and 26.0 mA/cm^2 (for the FTO-based PSC) to 29.4 mA/cm^2 (for the IO:H-based PSC). The J–V scans of the same PSCs (Figure 3c) also exhibit an improvement in the J_{SC} values of the IO:H-based PSC by ≈2 and 3 mA/cm^2 compared to the ITO- and FTO-based PSCs, respectively. The high J_{SC} is indicative of effective hole extractions by the TCOs (ITO, FTO, and IO:H) even in the absence of an HTL.

As discussed earlier, the higher transmittance of IO:H in the NIR region stems from lower charge carrier concentration (n_c) (compared to ITO and FTO), which is accompanied by a higher R_{sq} and therefore lower FF. This consequently affects the overall performance of the IO:H-based PSCs despite their significantly higher J_{SC}. Statistical analysis is necessary to verify a real improvement in the device performance after a given change.[58] Here, the J–V characteristics from 40 identically prepared PSCs of each TCO shows slightly higher PCE for the HTL-free NBG PSCs fabricated on IO:H substrates compared to those fabricated on ITO (Figure S9). Although the J_{SC} of IO:H-based PSCs is higher than that of the ITO-based PSCs by ≈2 mA/cm^2, on average, the higher FF of the ITO-based devices compensate for the lower currents. Moreover, for all three TCOs, HTL-free PSCs generate reasonable V_{OC} despite the lack of a selective HTL contact. We speculate that the missing HTL is not affecting the alignment of the energy band at the TCO/perovskite interface significantly, as previously shown for ITO-based devices in Figure S1. It should be noted that FTO-based PSCs show severe hysteresis (Figure 3b) that could be initiated by ion migration at the FTO/perovskite interface.[59] Table 2 summarizes the J–V characteristics of the champion PSCs with different TCOs. As MPP tracking measurements (Figure 3d) show, removing the HTL is not detrimental to the SPCE of these solar cells with different TCOs.

https://doi.org/10.1021/acsami.1c06457
ACS Appl. Mater. Interfaces XXXX, XXX, XXX–XXX

Table 2. Short-Circuit Current (J_{SC}), Open-Circuit Voltage (V_{OC}), Fill Factor (FF), and Power Conversion Efficiency (PCE) Derived from Current Density−Voltage Characteristics, Stabilized Power Conversion Efficiency (SPCE) from Maximum Power Point Tracking Measurements, and J_{SC} Values Integrated from External Quantum Efficiency (EQE) Spectra of Champion HTL-Free NBG PSCs with Different Transparent Conductive Oxide Electrodes (ITO, FTO, and IO:H)

PV characteristics	scan direction	ITO	FTO	IO:H
J_{SC} (mA/cm^2)	backward	28.5	27.2	30.5
	forward	28.3	26.8	30.4
V_{OC} (mV)	backward	804	768	787
	forward	796	722	777
FF (%)	backward	74.6	72.5	72.1
	forward	66.3	57.5	61.7
PCE (%)	backward	17.1	15.1	17.3
	forward	14.9	11.1	14.6
SPCE (%)		16.5	14.7	17.0
J_{sc} (mA/cm^2) integrated from EQE		27.5	26.0	29.4

The performance of the bottom subcell in a 4T tandem solar cell is correlated with the choice of the front and rear TCO electrodes of the semitransparent top subcell. Here, we fabricate semitransparent top PSCs on ITO and IO:H front electrodes for use in combination with ITO- and IO:H-based HTL-free NBG bottom subcells in 4T all-PTSC configurations. As illustrated in Figure 4a,b, the devices are categorized as ITO-based and IO:H-based 4T all-PTSCs with top and bottom subcells both deposited on ITO and IO:H, respectively. A 165 nm sputtered indium zinc oxide (IZO) layer ($R_{sq} \approx 60$ Ω/sq) serves as the rear electrode of the semitransparent top subcell in both stacks (see Table S1 for the sputtering parameters). As shown in Figure S10, spectrophotometric measurements conducted on glass/IZO/air show that the NIR absorptance of this layer is very low (<5%). According to the findings presented in our previous study,[44] the rear electrode of the top subcell in a tandem device has a significant influence on the reflection and absorption in the NIR wavelengths. Thin IZO rear electrodes result in high NIR reflection and limit the PCE of the top PSC with a high series resistance, while thicker layers reduce the tandem performance due to high NIR absorption. Overall, a combination of a 165 nm IZO rear electrode and a 230 nm IO:H front electrode in the top PSC achieved the best trade-off between the electrical and optical restrictions,[40,44] which is consequently used in this study.

The semitransparent top PSC has a triple-cation perovskite absorber layer with a band gap of 1.62 eV and a layer sequence of glass/TCO (ITO or IO:H)/nanoparticles of SnO_2 (np-SnO_2)/$Cs_{0.1}(FA_{0.83}MA_{0.17})_{0.9}Pb(I_{0.83}Br_{0.17})_3$/2,20,7,70-tetrakis-[*N*,*N*-di(4-methoxyphenyl)amino]-9,90-spirobifluorene (spiro-MeOTAD)/molybdenum oxide (MoO_x)/IZO/magnesium fluoride (MgF_2) (see the Supporting Information for more details). A 10 nm buffer layer of MoO_x is to protect the spiro-MeOTAD against the ion bombardment during the sputtering process of the IZO rear electrode. Moreover, as studied in our previous publication,[6] a thin film (165 nm) of MgF_2 on the rear electrode acts as an antireflection coating and enhances the transmission of the semitransparent top PSC (in the wavelength range of 700−1200 nm). We attribute this enhancement to a gradual drop in the refractive index through the layer stack of IZO/MgF_2/air (2.0/1.4/1.0), instead of an abrupt step, as in the case of the IZO/air interface.[60]

Figure 4c,d exhibits that, as expected, replacing the ITO front electrodes with IO:H in both subcells results in an increase in the J_{SC} from 20.2 to 20.8 mA/cm^2 (for the semitransparent top PSC) and from 28.5 to 30.5 mA/cm^2 (for the HTL-free NBG bottom PSC). The remarkably enhanced J_{SC} enables the IO:H-based PSCs to maintain PCEs of up to 19.0% (top PSC) and 17.3% (bottom PSC), compared to their ITO-based counterparts with PCEs of 18.2% (top PSC) and 17.1% (bottom PSC). To evaluate the filtered NBG bottom PSCs, we use ITO- and IO:H-based semitransparent perovskite filters on top of the NBG bottom PSCs with the same front electrodes. The ITO- and IO:H-based semitransparent perovskite filters (substrate area of 225 mm^2) are fabricated under identical conditions and have the same layer stacking as the semitransparent top PSCs. The IO:H-based (ITO-based) HTL-free NBG bottom PSC exhibits a PCE of 5.8% (5.1%) when filtered with an IO:H-based (ITO-based) semitransparent filter. This improvement is a consequence of a boost in the J_{SC} from 8.5 mA/cm^2 (for the ITO-based NBG bottom PSC) to 10.5 mA/cm^2 (for the IO:H-based NBG bottom PSC) when filtered by an ITO- and an IO:H-based filter, respectively. Adding the PCEs of the top subcells to those of the filtered bottom PSCs, we determine a significant improvement in the PCE from 23.3% (=18.2 + 5.1%) for an ITO/ITO 4T all-PTSC to 24.8% (=19.0 + 5.8%) for an IO:H/IO:H 4T all-PTSC. Table 3 summarizes all of the PV parameters of the top and bottom subcells and their respective 4T all-PTSCs. Moreover, the SPCE of the 4T all-PTSCs from the MPP tracking for over 300 s (Figure 4e,f) is calculated by adding the SPCEs of the top PSC and the filtered NBG bottom PSCs. The IO:H/IO:H 4T all-PTSC attains an SPCE of 23.3% outperforming that of an ITO/ITO 4T all-PTSC with an SPCE of 21.9%.

Notably, the V_{OC} of the ITO-based bottom PSC decreases when filtered with an ITO-based perovskite filter. We explain this observation by the logarithmic dependency of the V_{OC} on the light intensity.[61] Under filtration conditions, particularly using an ITO-based filter, the intensity of the light that reaches the bottom PSC is reduced, which can potentially result in a reduction in the V_{OC} of the bottom PSC.

Regarding the optical performance of the semitransparent top PSCs, we evaluated the absorptance, reflectance, and transmittance of the ITO- and IO:H-based semitransparent perovskite filters, as shown in Figure S11. As intended, the use of IO:H leads to a significant increase in the transmittance and a reduction in the absorptance over the NIR region, which increases the share of the solar spectrum reached by the bottom PSC. Notably, the device with ITO exhibits a strong reflectance (∼10%) in this region (>900 nm) due to the high charge carrier concentration (n_c) of the ITO compared to IO:H (see Table 1).

Furthermore, similar to the NBG bottom PSCs, replacing the ITO front electrode with IO:H results in an overall enhancement in the EQE spectra (accompanied by the enhanced absorptance) of the semitransparent top PSCs (Figure S11a) in the wavelength region from 500 nm to the band gap (760 nm) of the perovskite. This enhancement in the absorptance is enabled by the low reflection loss (∼5%) at the IO:H/perovskite interface in this region (Figure S11b). The EQE of the ITO-based bottom PSC when filtered by the ITO-

https://doi.org/10.1021/acsami.1c06457
ACS Appl. Mater. Interfaces XXXX, XXX, XXX−XXX

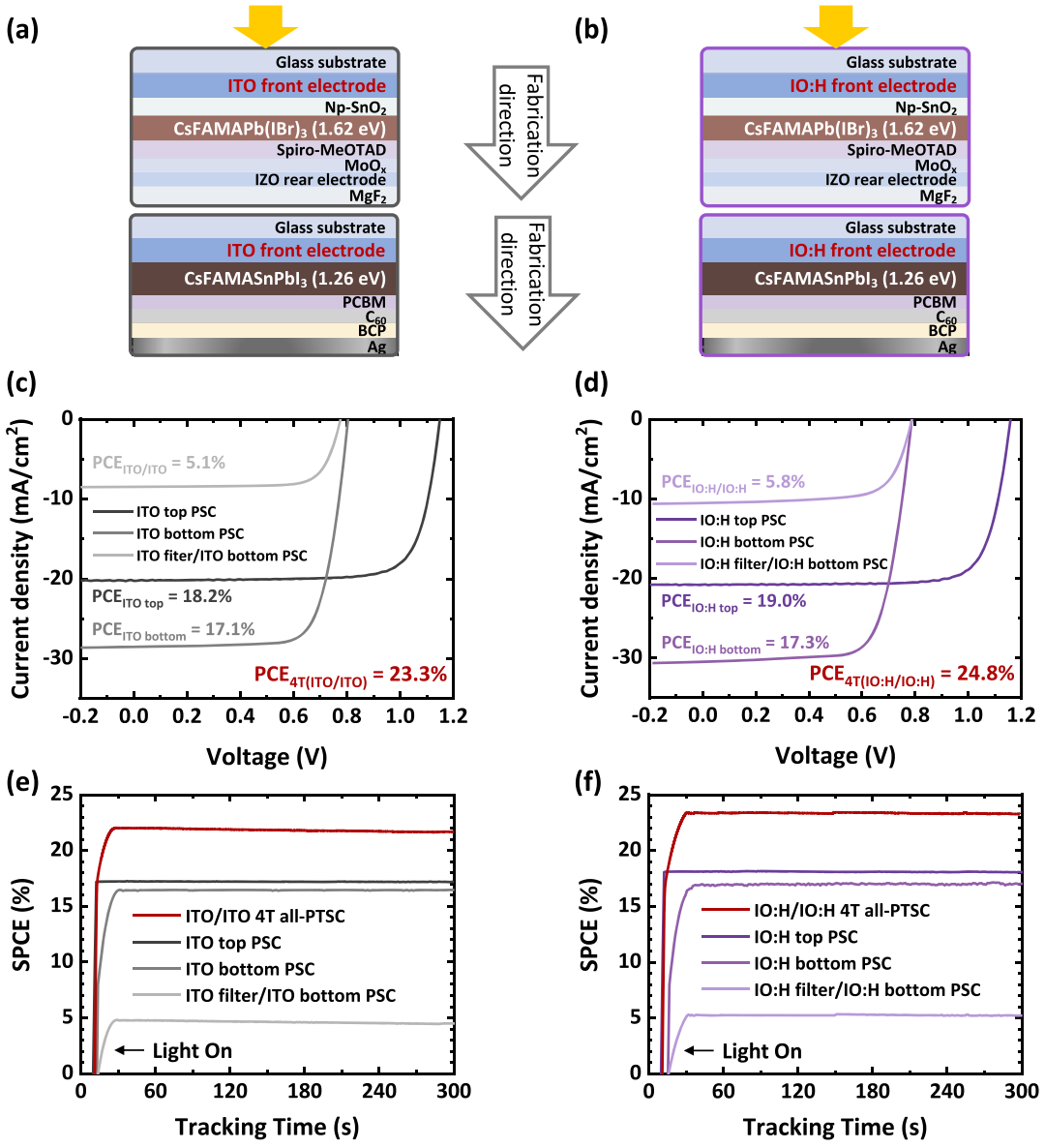

Figure 4. (a, b) Schematic cross-sectional images, (c, d) current density vs voltage (J–V) scans (from backward scan ($V_{OC} \rightarrow J_{SC}$) at a fixed rate of 0.6 V/s), and (e, f) stabilized power conversion efficiency (SPCE) from maximum power point tracking measurements of the ITO- and IO:H-based (semitransparent top and HTL-free bottom) PSCs, respectively. The measurement was performed under the standard test conditions (100 mW/cm^2, 25 °C).

based PSC (Figure S11d), however, is limited by two factors: (1) the reduced NIR transmittance of the ITO-based top PSC (Figure S11c) that suppresses the EQE at longer wavelengths (around ≈870 nm) and (2) the reduced EQE of the ITO-based NBG bottom PSC itself (Figure 3b) due to low transmittance of its ITO front electrode compared to that of an IO:H-based NBG bottom PSC.

Furthermore, we determine the performance of the ITO/IO:H and IO:H/ITO 4T all-PTSCs by evaluating the performance of the ITO- and IO:H-based NBG bottom PSCs, while a semitransparent perovskite filter with the opposite front TCO electrode is applied on top (see the schematics in Figures S12a and S12b). From the J–V characteristics, shown in Figures S12c and S12d, we realize that the PCEs of both ITO- and IO:H-based bottom PSCs improve in the case where the ITO-based filter is replaced by the IO:H-based filter on top (from 5.1 to 5.6% for an ITO-based bottom PSC and from 5.3 to 5.8% for an IO:H-based bottom PSC). As expected, this improvement is a consequence of the enhanced J_{SC} and confirms that IO:H stands out as a beneficial front electrode in both subcells, resulting in a boost in the efficiency of the 4T all-PTSCs.

Further improving other PV characteristics of the IO:H-based subcells, such as hysteresis and FF, will be the focus of future studies. As mentioned earlier, the low charge carrier concentration (n_c) of the IO:H layer comes at a cost of high sheet resistance (R_{sq}) that, according to our previous study,[41] leads to poor FF of the corresponding PSCs. Increasing the thickness of the layer along with high charge carrier mobility (μ) compensates for the low charge carrier concentration, and therefore decreases the sheet resistance. Since there is an optimum threshold for the thickness, depositing highly crystalline IO:H layers with less grain boundary defects leading to even higher charge carrier mobility is essential for

https://doi.org/10.1021/acsami.1c06457
ACS Appl. Mater. Interfaces XXXX, XXX, XXX−XXX

Table 3. Photovoltaic Parameters of Champion ITO- and IO:H-Based Semitransparent Top and HTL-Free Bottom Perovskite Solar Cells (Stand-alone and Filtered by ITO- and IO:H-Based Filters) Derived from $J-V$ Measurements (Backward Scans: Top Rows and Forward Scans: Bottom Rows)[a]

ITO-based perovskite solar cell	J_{SC}(mA/cm^2)	V_{OC} (mV)	FF (%)	PCE (%)	SPCE (%)
Semitransparent top	20.2	1149	78.2	**18.2**	**17.3**
	20.1	1108	70.1	**15.6**	
HTL-free bottom (stand-alone)	28.5	805	74.6	17.1	16.5
	28.3	796	66.3	14.9	
HTL-free bottom (filtered by ITO-based top PSC)	8.5	776	76.6	**5.1**	**4.6**
	8.4	769	68.8	**4.4**	
ITO/ITO 4T all-PTSC				**23.3**	**21.9**
				20.0	
IO:H-based perovskite solar cell	**J_{SC} (mA/cm^2)**	**V_{OC} (mV)**	**FF (%)**	**PCE (%)**	**SPCE (%)**
Semitransparent top	20.8	1159	78.7	**19**	**18.1**
	20.7	1134	73.9	**17.4**	
HTL-free bottom (stand-alone)	30.5	787	72.1	17.3	17.0
	30.4	777	61.7	14.6	
HTL-free bottom (filtered by IO:H-based top PSC)	10.5	788	70.2	**5.8**	**5.2**
	10.4	777	62.9	**5.1**	
IO:H/IO:H 4T all-PTSC				**24.8**	**23.3**
				22.5	

[a]The stabilized PCE (SPCE) of the top and bottom (stand-alone and filtered) PSCs and that calculated, respectively, for the 4T all-PTSC are in bold.

reducing the sheet resistance and consequently enhance FF of the corresponding PSCs. Introducing H_2O vapors into a chamber during the sputtering process, for incorporating an H-donor into the In_2O_3 matrix, has been suggested to further suppress the formation of grain boundary defects resulting in highly crystalline IO:H layers with quite high charge carrier mobilities and significant optical performance.[33]

Apart from high PV performances, all-perovskite tandem photovoltaics have the potential for low material and fabrication costs, in particular, because of the low-investment deposition systems.[62] Thereby, as will be discussed in the following, the costs of a certain architecture should always be considered along with the PV performance. Although replacing the commonly used ITO front electrode with IO:H in both subcells increases the PCE of our tandem solar cells significantly by 1.5% (absolute), the associated costs remain unknown as IO:H is not yet used in large-scale PV production. A first rough estimate based on laboratory-scale prices of sputter targets (see Table S3) suggests that IO:H electrodes double the costs for the transparent electrodes. Moreover, the architecture should be modified such that the NBG PSC is processed in a substrate configuration. Otherwise, an additional back cover glass is required for the production of solar cell modules, which would make the architecture economically unfeasible due to a cost increase of around €10/m^2.[63] Thus, architectures that require only two glass layers (a front glass substrate and a back cover glass), such as monolithic all-perovskite tandem solar cells,[8,10,12,13] are desirable to prevent unnecessary costs. Such devices, with a current record efficiency of 24.8%,[10] offer avenues for making low-cost combined with high-efficiency all-perovskite tandem PV technologies and should be the focus of further studies.

CONCLUSIONS

In summary, we compare the optical and electrical properties of in-house sputtered IO:H with the commonly used commercial ITO and FTO transparent conductive oxides. IO:H shows significantly higher transmittance, especially in the NIR wavelengths. X-ray photoelectron spectroscopy indicates that, in comparison with ITO and FTO substrates, the growth of the narrow-band gap mixed Sn−Pb perovskite is faster on the Sn-O free IO:H substrate and less Sn^{4+} formation at the IO:H/perovskite interface occurs. Implementing highly transparent IO:H electrodes with nearly zero parasitic absorption (<2%), we design IO:H-based HTL-free PSCs with a narrow-band gap mixed Sn−Pb perovskite thin film deposited directly on the IO:H front electrode as well as semitransparent top PSCs. The use of IO:H instead of ITO as the front electrode enables us to fabricate IO:H-based 4T all-PTSCs with PCE as high as 24.8%, outperforming the ITO-based 4T all-PTSCs with a PCE of 23.3%. To the best of our knowledge, this is the first study on the IO:H-based all-perovskite tandem solar cells as well as an HTL-free narrow-band gap perovskite solar cell serving as the bottom subcell.

ASSOCIATED CONTENT

Supporting Information

The Supporting Information is available free of charge at https://pubs.acs.org/doi/10.1021/acsami.1c06457.

Supporting Figures, materials, fabrication methods, and characterization of the thin films and devices (PDF)

AUTHOR INFORMATION

Corresponding Authors

Bahram Abdollahi Nejand − *Light Technology Institute (LTI), Karlsruhe Institute of Technology, 76131 Karlsruhe, Germany; Institute of Microstructure Technology (IMT), Karlsruhe Institute of Technology, 76344 Eggenstein-Leopoldshafen, Germany;* orcid.org/0000-0001-9426-1217; Email: bahram.abdollahi@kit.edu

Ulrich W. Paetzold − *Light Technology Institute (LTI), Karlsruhe Institute of Technology, 76131 Karlsruhe, Germany; Institute of Microstructure Technology (IMT), Karlsruhe Institute of Technology, 76344 Eggenstein-*

https://doi.org/10.1021/acsami.1c06457
ACS Appl. Mater. Interfaces XXXX, XXX, XXX−XXX

Leopoldshafen, Germany; orcid.org/0000-0002-1557-8361; Email: ulrich.paetzold@kit.edu

Authors

Somayeh Moghadamzadeh – *Light Technology Institute (LTI), Karlsruhe Institute of Technology, 76131 Karlsruhe, Germany; Institute of Microstructure Technology (IMT), Karlsruhe Institute of Technology, 76344 Eggenstein-Leopoldshafen, Germany;* orcid.org/0000-0002-9120-6746

Ihteaz M. Hossain – *Light Technology Institute (LTI), Karlsruhe Institute of Technology, 76131 Karlsruhe, Germany; Institute of Microstructure Technology (IMT), Karlsruhe Institute of Technology, 76344 Eggenstein-Leopoldshafen, Germany;* orcid.org/0000-0001-6533-1757

Moritz Loy – *Center for Solar Energy and Hydrogen Research Baden-Württemberg (ZSW), Stuttgart 70563, Germany;* orcid.org/0000-0001-8921-1055

David Benedikt Ritzer – *Light Technology Institute (LTI), Karlsruhe Institute of Technology, 76131 Karlsruhe, Germany; Institute of Microstructure Technology (IMT), Karlsruhe Institute of Technology, 76344 Eggenstein-Leopoldshafen, Germany;* orcid.org/0000-0002-3301-6688

Hang Hu – *Light Technology Institute (LTI), Karlsruhe Institute of Technology, 76131 Karlsruhe, Germany; Institute of Microstructure Technology (IMT), Karlsruhe Institute of Technology, 76344 Eggenstein-Leopoldshafen, Germany;* orcid.org/0000-0001-8141-8772

Dirk Hauschild – *Institute for Photon Science and Synchrotron Radiation (IPS), Karlsruhe Institute of Technology, 76344 Eggenstein-Leopoldshafen, Germany; Institute for Chemical Technology and Polymer Chemistry (ITCP), Karlsruhe Institute of Technology, 76128 Karlsruhe, Germany;* orcid.org/0000-0001-9088-8944

Adrian Mertens – *Light Technology Institute (LTI), Karlsruhe Institute of Technology, 76131 Karlsruhe, Germany; Institute of Microstructure Technology (IMT), Karlsruhe Institute of Technology, 76344 Eggenstein-Leopoldshafen, Germany;* orcid.org/0000-0003-3891-5161

Jan-Philipp Becker – *Center for Solar Energy and Hydrogen Research Baden-Württemberg (ZSW), Stuttgart 70563, Germany;* orcid.org/0000-0001-5668-1544

Amir A. Haghighirad – *Institute for Quantum Materials and Technologies (IQMT), Karlsruhe Institute of Technology, 76344 Eggenstein-Leopoldshafen, Germany;* orcid.org/0000-0003-4723-4966

Erik Ahlswede – *Center for Solar Energy and Hydrogen Research Baden-Württemberg (ZSW), Stuttgart 70563, Germany;* orcid.org/0000-0001-8782-136X

Lothar Weinhardt – *Institute for Photon Science and Synchrotron Radiation (IPS), Karlsruhe Institute of Technology, 76344 Eggenstein-Leopoldshafen, Germany; Institute for Chemical Technology and Polymer Chemistry (ITCP), Karlsruhe Institute of Technology, 76128 Karlsruhe, Germany;* orcid.org/0000-0003-3361-1054

Uli Lemmer – *Light Technology Institute (LTI), Karlsruhe Institute of Technology, 76131 Karlsruhe, Germany; Institute of Microstructure Technology (IMT), Karlsruhe Institute of Technology, 76344 Eggenstein-Leopoldshafen, Germany;* orcid.org/0000-0001-9892-329X

Complete contact information is available at: https://pubs.acs.org/10.1021/acsami.1c06457

Author Contributions

S.M. wrote the first draft of the manuscript. S.M. and B.A.N. developed the idea and designed the experiments of this study. B.A.N. and U.W.P. supervised this work. S.M. fabricated and characterized the triple-cation narrow-band gap PSCs together with H.H. The triple-cation semitransparent PSCs with different TCOs were designed by S.M. and I.M.H. who fabricated the devices and contributed to performing characterization of TCOs as well. M.L. and J.P.B. developed the sputtering process of the IO:H substrates (in ZSW) supervised by E.A. The in-house IO:H substrates were patterned by D.B.R. using pulsed laser ablation for the cell area definition. A.M. conducted the ellipsometry measurements on the TCOs followed by detailed analyses. D.H. and L.W. conducted the XPS measurements (in IPS) and contributed to the discussion on photospectroscopy. A.A.H. contributed to the discussion regarding the XRD analysis. S.M., B.A.N., U.W.P., and U.L. concluded the discussion of the results. All authors contributed to writing the final version of the manuscript

Funding

S.M. received funding from DAAD (Deutscher Akademischer Austauschdienst/German academic exchange service) for her doctoral research work under personal reference number 91621525. H.H. received funding from the China Scholarship Council (CSC) for his doctoral research work (CSC number: 201808420221). D.H. and L.W. received funding from the Deutsche Forschungsgemeinschaft (DFG) for the MFE lab instrumentation in project GZ: INST 121384/64-1 FUGG. B.A.N. received funding from European Union's Horizon 2020 research and innovation program under the Marie Skłodowska-Curie (grant agreement number: 840937). U.W.P. received funding from the German Federal Ministry of Education and Research (BMBF) through the PRINTPERO project (funding code: 03SF0557A), and the German Federal Ministry for Economic Affairs and Energy through CAPITANO project (funding code: 03EE1038B).

Notes

The authors declare no competing financial interest.

■ ACKNOWLEDGMENTS

The authors acknowledge Yidenekachew Donie for the AFM measurements. The support from the Karlsruhe School of Optics & Photonics (KSOP) is gratefully acknowledged.

■ REFERENCES

(1) NREL Best-Research-Cell-Efficiencies.20201228.Pdf.

(2) Shockley, W.; Queisser, H. J. Detailed Balance Limit of Efficiency of P-n Junction Solar Cells. *J. Appl. Phys.* **1961**, *32*, 510–519.

(3) Hörantner, M. T.; Snaith, H. J. Predicting and Optimising the Energy Yield of Perovskite-on-Silicon Tandem Solar Cells under Real World Conditions. *Energy Environ. Sci.* **2017**, *10*, 1983–1993.

(4) Hörantner, M. T.; Leijtens, T.; Ziffer, M. E.; Eperon, G. E.; Christoforo, M. G.; McGehee, M. D.; Snaith, H. J. The Potential of Multijunction Perovskite Solar Cells. *ACS Energy Lett.* **2017**, *2*, 2506–2513.

(5) Futscher, M. H.; Ehrler, B. Efficiency Limit of Perovskite/Si Tandem Solar Cells. *ACS Energy Lett.* **2016**, *1*, 863–868.

(6) Gharibzadeh, S.; Hossain, I. M.; Fassl, P.; Nejand, B. A.; Abzieher, T.; Schultes, M.; Ahlswede, E.; Jackson, P.; Powalla, M.; Schäfer, S.; Rienäcker, M.; Wietler, T.; Peibst, R.; Lemmer, U.;

Richards, B. S.; Paetzold, U. W. 2D/3D Heterostructure for Semitransparent Perovskite Solar Cells with Engineered Bandgap Enables Efficiencies Exceeding 25% in Four-Terminal Tandems with Silicon and CIGS. *Adv. Funct. Mater.* **2020**, *30*, No. 1909919.
(7) Lehr, J.; Langenhorst, M.; Schmager, R.; Kirner, S.; Lemmer, U.; Richards, B. S.; Case, C.; Paetzold, U. W. Energy Yield Modelling of Perovskite/Silicon Two-Terminal Tandem PV Modules with Flat and Textured Interfaces. *Sustainable Energy Fuels* **2018**, *2*, 2754−2761.
(8) Xiao, K.; Lin, R.; Han, Q.; Hou, Y.; Qin, Z.; Nguyen, H. T.; Wen, J.; Wei, M.; Yeddu, V.; Saidaminov, M. I.; Gao, Y.; Luo, X.; Wang, Y.; Gao, H.; Zhang, C.; Xu, J.; Zhu, J.; Sargent, E. H.; Tan, H. All-Perovskite Tandem Solar Cells with 24.2% Certified Efficiency and Area over 1 Cm2 Using Surface-Anchoring Zwitterionic Antioxidant. *Nat. Energy* **2020**, *5*, 870−880.
(9) Tong, J.; Song, Z.; Kim, D. H.; Chen, X.; Chen, C.; Palmstrom, A. F.; Ndione, P. F.; Reese, M. O.; Dunfield, S. P.; Reid, O. G.; Liu, J.; Zhang, F.; Harvey, S. P.; Li, Z.; Christensen, S. T.; Teeter, G.; Zhao, D.; Al-Jassim, M. M.; van Hest, M. F. A. M.; Beard, M. C.; Shaheen, S. E.; Berry, J. J.; Yan, Y.; Zhu, K. Carrier Lifetimes of >1 μs in Sn-Pb Perovskites Enable Efficient All-Perovskite Tandem Solar Cells. *Science* **2019**, *364*, 475−479.
(10) Lin, R.; Xiao, K.; Qin, Z.; Han, Q.; Zhang, C.; Wei, M.; Saidaminov, M. I.; Gao, Y.; Xu, J.; Xiao, M.; Li, A.; Zhu, J.; Sargent, E. H.; Tan, H. Monolithic All-Perovskite Tandem Solar Cells with 24.8% Efficiency Exploiting Comproportionation to Suppress Sn(II) Oxidation in Precursor Ink. *Nat. Energy* **2019**, *4*, 864−873.
(11) Wang, C.; Song, Z.; Li, C.; Zhao, D.; Yan, Y. Low-Bandgap Mixed Tin-Lead Perovskites and Their Applications in All-Perovskite Tandem Solar Cells. *Adv. Funct. Mater.* **2019**, *29*, No. 1808801.
(12) Yang, Z.; Yu, Z.; Wei, H.; Xiao, X.; Ni, Z.; Chen, B.; Deng, Y.; Habisreutinger, S. N.; Chen, X.; Wang, K.; Zhao, J.; Rudd, P. N.; Berry, J. J.; Beard, M. C.; Huang, J. Enhancing Electron Diffusion Length in Narrow-Bandgap Perovskites for Efficient Monolithic Perovskite Tandem Solar Cells. *Nat. Commun.* **2019**, *10*, No. 4498.
(13) Zhao, D.; Chen, C.; Wang, C.; Junda, M. M.; Song, Z.; Grice, C. R.; Yu, Y.; Li, C.; Subedi, B.; Podraza, N. J.; Zhao, X.; Fang, G.; Xiong, R.-G.; Zhu, K.; Yan, Y. Efficient Two-Terminal All-Perovskite Tandem Solar Cells Enabled by High-Quality Low-Bandgap Absorber Layers. *Nat. Energy* **2018**, *3*, 1093−1100.
(14) Leijtens, T.; Bush, K. A.; Prasanna, R.; McGehee, M. D. Opportunities and Challenges for Tandem Solar Cells Using Metal Halide Perovskite Semiconductors. *Nat. Energy* **2018**, *3*, 828−838.
(15) Correa-Baena, J.-P.; Saliba, M.; Buonassisi, T.; Grätzel, M.; Abate, A.; Tress, W.; Hagfeldt, A. Promises and Challenges of Perovskite Solar Cells. *Science* **2017**, *358*, 739−744.
(16) Jiang, T.; Chen, Z.; Chen, X.; Liu, T.; Chen, X.; Sha, W. E. I.; Zhu, H.; Yang, Y. Michael. Realizing High Efficiency over 20% of Low-Bandgap Pb−Sn-Alloyed Perovskite Solar Cells by In Situ Reduction of Sn 4+. *Sol. RRL* **2020**, *4*, No. 1900467.
(17) Kapil, G.; Bessho, T.; Ng, C. H.; Hamada, K.; Pandey, M.; Kamarudin, M. A.; Hirotani, D.; Kinoshita, T.; Minemoto, T.; Shen, Q.; Toyoda, T.; Murakami, T. N.; Segawa, H.; Hayase, S. Strain Relaxation and Light Management in Tin−Lead Perovskite Solar Cells to Achieve High Efficiencies. *ACS Energy Lett.* **2019**, *4*, 1991−1998.
(18) Ratcliff, E. L.; Meyer, J.; Steirer, K. X.; Garcia, A.; Berry, J. J.; Ginley, D. S.; Olson, D. C.; Kahn, A.; Armstrong, N. R. Evidence for Near-Surface NiOOH Species in Solution-Processed NiO x Selective Interlayer Materials: Impact on Energetics and the Performance of Polymer Bulk Heterojunction Photovoltaics. *Chem. Mater.* **2011**, *23*, 4988−5000.
(19) Abdollahi Nejand, B.; Hossain, I. M.; Jakoby, M.; Moghadamzadeh, S.; Abzieher, T.; Gharibzadeh, S.; Schwenzer, J. A.; Nazari, P.; Schackmar, F.; Hauschild, D.; Weinhardt, L.; Lemmer, U.; Richards, B. S.; Howard, I. A.; Paetzold, U. W. Vacuum-Assisted Growth of Low-Bandgap Thin Films (FA 0.8 MA 0.2 Sn 0.5 Pb 0.5 I 3) for All-Perovskite Tandem Solar Cells. *Adv. Energy Mater.* **2020**, *10*, No. 1902583.
(20) Moghadamzadeh, S.; Hossain, I. M.; Duong, T.; Gharibzadeh, S.; Abzieher, T.; Pham, H.; Hu, H.; Fassl, P.; Lemmer, U.; Nejand, B. A.; Paetzold, U. W. Triple-Cation Low-Bandgap Perovskite Thin-Films for High-Efficiency Four-Terminal All-Perovskite Tandem Solar Cells. *J. Mater. Chem. A* **2020**, *8*, 24608−24619.
(21) Prasanna, R.; Leijtens, T.; Dunfield, S. P.; Raiford, J. A.; Wolf, E. J.; Swifter, S. A.; Werner, J.; Eperon, G. E.; de Paula, C.; Palmstrom, A. F.; Boyd, C. C.; van Hest, M. F. A. M.; Bent, S. F.; Teeter, G.; Berry, J. J.; McGehee, M. D. Design of Low Bandgap Tin−Lead Halide Perovskite Solar Cells to Achieve Thermal, Atmospheric and Operational Stability. *Nat. Energy* **2019**, *4*, 939−947.
(22) Werner, J.; Moot, T.; Gossett, T. A.; Gould, I. E.; Palmstrom, A. F.; Wolf, E. J.; Boyd, C. C.; van Hest, M. F. A. M.; Luther, J. M.; Berry, J. J.; McGehee, M. D. Improving Low-Bandgap Tin−Lead Perovskite Solar Cells via Contact Engineering and Gas Quench Processing. *ACS Energy Lett.* **2020**, *5*, 1215−1223.
(23) Bi, C.; Wang, Q.; Shao, Y.; Yuan, Y.; Xiao, Z.; Huang, J. Non-Wetting Surface-Driven High-Aspect-Ratio Crystalline Grain Growth for Efficient Hybrid Perovskite Solar Cells. *Nat. Commun.* **2015**, *6*, No. 7747.
(24) Liu, X.; Cheng, Y.; Liu, C.; Zhang, T.; Zhang, N.; Zhang, S.; Chen, J.; Xu, Q.; Ouyang, J.; Gong, H. 20.7% Highly Reproducible Inverted Planar Perovskite Solar Cells with Enhanced Fill Factor and Eliminated Hysteresis. *Energy Environ. Sci.* **2019**, *12*, 1622−1633.
(25) Petrović, M.; Maksudov, T.; Panagiotopoulos, A.; Serpetzoglou, E.; Konidakis, I.; Stylianakis, M. M.; Stratakis, E.; Kymakis, E. Limitations of a Polymer-Based Hole Transporting Layer for Application in Planar Inverted Perovskite Solar Cells. *Nanoscale Adv.* **2019**, *1*, 3107−3118.
(26) Khadka, D. B.; Shirai, Y.; Yanagida, M.; Ryan, J. W.; Miyano, K. Exploring the Effects of Interfacial Carrier Transport Layers on Device Performance and Optoelectronic Properties of Planar Perovskite Solar Cells. *J. Mater. Chem. C* **2017**, *5*, 8819−8827.
(27) Lv, F.; Yao, Y.; Xu, C.; Liu, D.; Liao, L.; Wang, G.; Zhou, G.; Zhao, X.; Liu, D.; Yang, X.; Song, Q. Elimination of Charge Transport Layers in High-Performance Perovskite Solar Cells by Band Bending. *ACS Appl. Energy Mater.* **2021**, *4*, 1294−1301.
(28) Kong, W.; Li, W.; Liu, C.; Liu, H.; Miao, J.; Wang, W.; Chen, S.; Hu, M.; Li, D.; Amini, A.; Yang, S.; Wang, J.; Xu, B.; Cheng, C. Organic Monomolecular Layers Enable Energy-Level Matching for Efficient Hole Transporting Layer Free Inverted Perovskite Solar Cells. *ACS Nano* **2019**, *13*, 1625−1634.
(29) Marshall, K. P.; Walker, M.; Walton, R. I.; Hatton, R. A. Enhanced Stability and Efficiency in Hole-Transport-Layer-Free CsSnI3 Perovskite Photovoltaics. *Nat. Energy* **2016**, *1*, No. 16178.
(30) Zhang, Y.; Hu, X.; Chen, L.; Huang, Z.; Fu, Q.; Liu, Y.; Zhang, L.; Chen, Y. Flexible, Hole Transporting Layer-Free and Stable CH3NH3PbI3/PC61BM Planar Heterojunction Perovskite Solar Cells. *Org. Electron.* **2016**, *30*, 281−288.
(31) Liao, Y.; Jiang, X.; Zhou, W.; Shi, Z.; Li, B.; Mi, Q.; Ning, Z. Hole-Transporting Layer-Free Inverted Planar Mixed Lead-Tin Perovskite-Based Solar Cells. *Front. Optoelectron.* **2017**, *10*, 103−110.
(32) Abzieher, T.; Schwenzer, J. A.; Moghadamzadeh, S.; Sutterluti, F.; Hossain, I. M.; Pfau, M.; Lotter, E.; Hetterich, M.; Richards, B. S.; Lemmer, U.; Powalla, M.; Paetzold, U. W. Efficient All-Evaporated Pin -Perovskite Solar Cells: A Promising Approach Toward Industrial Large-Scale Fabrication. *IEEE J. Photovoltaics* **2019**, *9*, 1249−1257.
(33) Koida, T.; Fujiwara, H.; Kondo, M. Hydrogen-Doped In 2 O 3 as High-Mobility Transparent Conductive Oxide. *Jpn. J. Appl. Phys.* **2007**, *46*, L685−L687.
(34) Jiang, Y.; Feurer, T.; Carron, R.; Sevilla, G. T.; Moser, T.; Pisoni, S.; Erni, R.; Rossell, M. D.; Ochoa, M.; Hertwig, R.; Tiwari, A. N.; Fu, F. High-Mobility In2O3:H Electrodes for Four-Terminal Perovskite/CuInSe2 Tandem Solar Cells. *ACS Nano* **2020**, *14*, 7502−7512.
(35) Kuang, Y.; Macco, B.; Karasulu, B.; Ande, C. K.; Bronsveld, P. C. P.; Verheijen, M. A.; Wu, Y.; Kessels, W. M. M.; Schropp, R. E. I. Towards the Implementation of Atomic Layer Deposited In2O3:H in

https://doi.org/10.1021/acsami.1c06457
ACS Appl. Mater. Interfaces XXXX, XXX, XXX−XXX

Silicon Heterojunction Solar Cells. *Sol. Energy Mater. Sol. Cells* **2017**, *163*, 43−50.
(36) Dawood, Y. Z.; Mohammed, M. S.; Al-Hamdani, A. H. Characterization and Optimization of In2O3 Thin Films for Application in Heterojunction Silicon Solar Cells. *J. Mater. Sci. Eng. A* **2012**, *2*, 352−356.
(37) Jäger, T.; Romanyuk, Y. E.; Bissig, B.; Pianezzi, F.; Nishiwaki, S.; Reinhard, P.; Steinhauser, J.; Schwenk, J.; Tiwari, A. N. Improved Open-Circuit Voltage in Cu(In,Ga)Se 2 Solar Cells with High Work Function Transparent Electrodes. *J. Appl. Phys.* **2015**, *117*, No. 225303.
(38) Jäger, T.; Romanyuk, Y. E.; Nishiwaki, S.; Bissig, B.; Pianezzi, F.; Fuchs, P.; Gretener, C.; Döbeli, M.; Tiwari, A. N. Hydrogenated Indium Oxide Window Layers for High-Efficiency Cu(In,Ga)Se 2 Solar Cells. *J. Appl. Phys.* **2015**, *117*, No. 205301.
(39) Fu, F.; Feurer, T.; Jäger, T.; Avancini, E.; Bissig, B.; Yoon, S.; Buecheler, S.; Tiwari, A. N. Low-Temperature-Processed Efficient Semi-Transparent Planar Perovskite Solar Cells for Bifacial and Tandem Applications. *Nat. Commun.* **2015**, *6*, No. 8932.
(40) Schultes, M.; Helder, T.; Ahlswede, E.; Aygüler, M. F.; Jackson, P.; Paetel, S.; Schwenzer, J. A.; Hossain, I. M.; Paetzold, U. W.; Powalla, M. Sputtered Transparent Electrodes (IO:H and IZO) with Low Parasitic Near-Infrared Absorption for Perovskite−Cu(In,Ga)-Se2 Tandem Solar Cells. *ACS Appl. Energy Mater.* **2019**, *2*, 7823−7831.
(41) Zhang, D.; Verhees, W.; Dörenkämper, M.; Qiu, W.; Bakker, K.; Gutjahr, A.; Veenstra, S.; Gehlhaar, R.; Paetzold, U. W.; Soppe, W.; Romijn, I.; Geerligs, L. J.; Aernouts, T.; Weeber, A. Combination of Advanced Optical Modelling with Electrical Simulation for Performance Evaluation of Practical 4-Terminal Perovskite/c-Si Tandem Modules. *Energy Procedia* **2016**, *92*, 669−677.
(42) Chen, J.; Park, N. Causes and Solutions of Recombination in Perovskite Solar Cells. *Adv. Mater.* **2019**, *31*, No. 1803019.
(43) Anaya, M.; Correa-Baena, J. P.; Lozano, G.; Saliba, M.; Anguita, P.; Roose, B.; Abate, A.; Steiner, U.; Grätzel, M.; Calvo, M. E.; Hagfeldt, A.; Míguez, H. Optical Analysis of CH3NH3Sn:XPb1- XI3 Absorbers: A Roadmap for Perovskite-on-Perovskite Tandem Solar Cells. *J. Mater. Chem. A* **2016**, *4*, 11214−11221.
(44) Schultes, M. Four-Terminal Perovskite-CIGS Tandem Solar Cells with Improved Near-Infrared Response, Dissertation, Karlsruhe Institute of Technology (KIT), 2020.
(45) Ahmad, M. K.; Marzuki, N. A.; Soon, C. F.; Nafarizal, N.; Sanudin, R.; Suriani, A. B.; Mohamed, A.; Shimomura, M.; Murakami, K.; Mamat, M. H.; Malek, M. F. Effect of Anneal Temperature on Fluorine Doped Tin Oxide (FTO) Nanostructured Fabricated Using Hydrothermal Method. *AIP Conf. Proc.* **2017**, *1788*, No. 030044.
(46) Climent-Pascual, E.; Hames, B. C.; Moreno-Ramírez, J. S.; Álvarez, A. L.; Juarez-Perez, E. J.; Mas-Marza, E.; Mora-Seró, I.; de Andrés, A.; Coya, C. Influence of the Substrate on the Bulk Properties of Hybrid Lead Halide Perovskite Films. *J. Mater. Chem. A* **2016**, *4*, 18153−18163.
(47) Zhao, D.; Yu, Y.; Wang, C.; Liao, W.; Shrestha, N.; Grice, C. R.; Cimaroli, A. J.; Guan, L.; Ellingson, R. J.; Zhu, K.; Zhao, X.; Xiong, R.-G.; Yan, Y. Low-Bandgap Mixed Tin−Lead Iodide Perovskite Absorbers with Long Carrier Lifetimes for All-Perovskite Tandem Solar Cells. *Nat. Energy* **2017**, *2*, No. 17018.
(48) Kim, H. D.; Ohkita, H.; Benten, H.; Ito, S. Photovoltaic Performance of Perovskite Solar Cells with Different Grain Sizes. *Adv. Mater.* **2016**, *28*, 917−922.
(49) Ren, X.; Yang, Z.; Yang, D.; Zhang, X.; Cui, D.; Liu, Y.; Wei, Q.; Fan, H.; Liu, S. F. Modulating Crystal Grain Size and Optoelectronic Properties of Perovskite Films for Solar Cells by Reaction Temperature. *Nanoscale* **2016**, *8*, 3816−3822.
(50) Chen, B.; Yu, Z.; Liu, K.; Zheng, X.; Liu, Y.; Shi, J.; Spronk, D.; Rudd, P. N.; Holman, Z.; Huang, J. Grain Engineering for Perovskite/Silicon Monolithic Tandem Solar Cells with Efficiency of 25.4%. *Joule* **2019**, *3*, 177−190.
(51) Cai, F.; Yan, Y.; Yao, J.; Wang, P.; Wang, H.; Gurney, R. S.; Liu, D.; Wang, T. Ionic Additive Engineering Toward High-Efficiency Perovskite Solar Cells with Reduced Grain Boundaries and Trap Density. *Adv. Funct. Mater.* **2018**, *28*, No. 1801985.
(52) Haider, S. Z.; Anwar, H.; Jamil, Y.; Shahid, M. A Comparative Study of Interface Engineering with Different Hole Transport Materials for High-Performance Perovskite Solar Cells. *J. Phys. Chem. Solids* **2020**, *136*, No. 109147.
(53) Jeong, J.; Lee, J.; Lee, H.; Hyun, G.; Park, S.; Yi, Y.; Cho, S. W.; Lee, H. Energy Level Alignment and Hole Injection Property of Poly(9-Vinylcarbazole)/Indium Tin Oxide Interface. *Chem. Phys. Lett.* **2018**, *706*, 317−322.
(54) Weinhardt, L.; Hauschild, D.; Heske, C. Surface and Interface Properties in Thin-Film Solar Cells: Using Soft X-rays and Electrons to Unravel the Electronic and Chemical Structure. *Adv. Mater.* **2019**, *31*, No. 1806660.
(55) Hauschild, D.; Kreikemeyer-Lorenzo, D.; Jackson, P.; Friedlmeier, T. M.; Hariskos, D.; Reinert, F.; Powalla, M.; Heske, C.; Weinhardt, L. Impact of a RbF Postdeposition Treatment on the Electronic Structure of the CdS/Cu(In,Ga)Se 2 Heterojunction in High-Efficiency Thin-Film Solar Cells. *ACS Energy Lett.* **2017**, *2*, 2383−2387.
(56) Duncan, D. A.; Mendelsberg, R.; Mezher, M.; Horsley, K.; Rosenberg, S. G.; Blum, M.; Xiong, G.; Weinhardt, L.; Gloeckler, M.; Heske, C. A New Look at the Electronic Structure of Transparent Conductive Oxides-A Case Study of the Interface between Zinc Magnesium Oxide and Cadmium Telluride. *Adv. Mater. Interfaces* **2016**, *3*, No. 1600418.
(57) Kraut, E. A.; Grant, R. W.; Waldrop, J. R.; Kowalczyk, S. P. Precise Determination of the Valence-Band Edge in X-Ray Photoemission Spectra: Application to Measurement of Semiconductor Interface Potentials. *Phys. Rev. Lett.* **1980**, *44*, 1620−1623.
(58) Luber, E. J.; Buriak, J. M. Reporting Performance in Organic Photovoltaic Devices. *ACS Nano* **2013**, *7*, 4708−4714.
(59) Chen, B.; Yang, M.; Priya, S.; Zhu, K. Origin of J-V Hysteresis in Perovskite Solar Cells. *J. Phys. Chem. Lett.* **2016**, *7*, 905−917.
(60) Hossain, I. M. Semitransparent Perovskite Solar Cells for Perovskite-Based Tandem Photovoltaics. Doctoral dissertation, Karlsruhe Institute of Technology (KIT), 2021.
(61) Tress, W.; Yavari, M.; Domanski, K.; Yadav, P.; Niesen, B.; Correa Baena, J. P.; Hagfeldt, A.; Graetzel, M. Interpretation and Evolution of Open-Circuit Voltage, Recombination, Ideality Factor and Subgap Defect States during Reversible Light-Soaking and Irreversible Degradation of Perovskite Solar Cells. *Energy Environ. Sci.* **2018**, *11*, 151−165.
(62) Cai, M.; Wu, Y.; Chen, H.; Yang, X.; Qiang, Y.; Han, L. Cost-Performance Analysis of Perovskite Solar Modules. *Adv. Sci.* **2017**, *4*, No. 1600269.
(63) Sofia, S. E.; Mailoa, J. P.; Weiss, D. N.; Stanbery, B. J.; Buonassisi, T.; Peters, I. M. Economic Viability of Thin-Film Tandem Solar Modules in the United States. *Nat. Energy* **2018**, *3*, 387−394.

https://doi.org/10.1021/acsami.1c06457
ACS Appl. Mater. Interfaces XXXX, XXX, XXX−XXX